Chapter 6

Epitaxy of a Periodic Adsorbate Structure on d-Al-Ni-Co

While the last chapter focused on the question if the formation of an epitaxial quasicrystalline film is possible, epitaxy of a periodic structure on a quasicrystalline surface will be investigated in this chapter. Several elements have already been found to form a periodic lattice on a quasicrystalline substrate [9, 14, 15, 123]. Their growth has been termed epitaxial in the sense that high symmetry lines of the periodic lattice align with those of the quasicrystal to yield twinned domains with the rotational symmetry of the substrate. The formation of a sputter-induced periodic overlayer due to Al depletion in the topmost surface layers of quasicrystals is also explained by a coincidence of high symmetry directions of the two lattices [19-22, 122]. Consequently, all systems found in the literature only concentrate on the directional relationships of the lattices at the interface, but not on the atomic structure in more detail. Therefore, the question how a long-range ordered interface can be achieved has not been fully addressed yet.

In this chapter, deposition of arsenic (As) onto the tenfold surface of d-Al-Ni-Co will be investigated. First, the adsorption process is monitored by helium atom scattering (HAS), before the resulting structure upon heating is resolved by a combination of helium and electron diffraction. Subsequently, the interface is investigated in detail. The term epitaxy will be extended for interfaces between periodic and quasiperiodic lattices, to yield a simple criterion for this growth mode in reciprocal space. This concept will first be discussed in a one-dimensional example: the interface between a periodic chain and a Fibonacci sequence. On this basis, the importance of a periodic average structure of quasicrystals will be illustrated before it will be applied to the experimentally investigated structure on d-Al-Ni-Co.
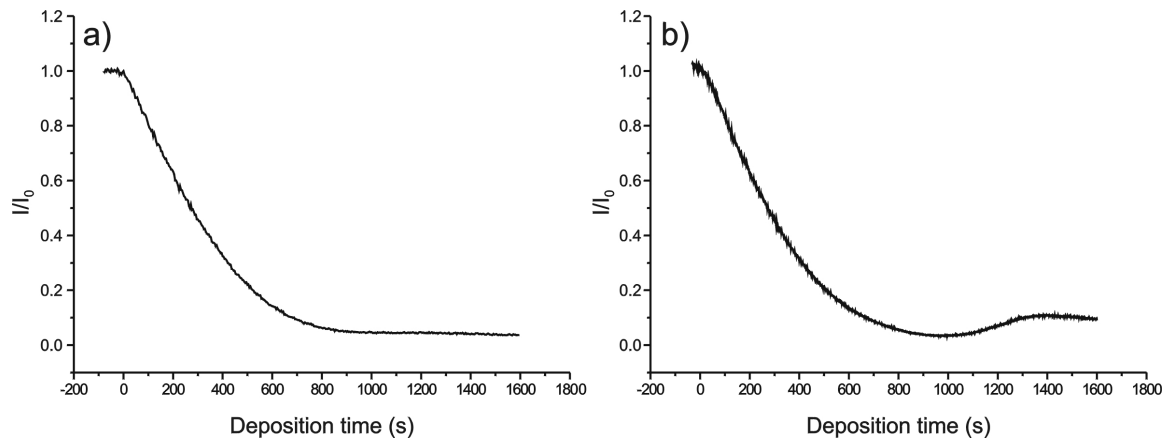
Figure 6.1: Adsorption curves of As at constant flux on the tenfold surface of d-Al-Ni-Co with the sample at (a) room temperature, and (b) at about $200\,°\text{C}$.

6.1   Facet Preparation and Temperature Dependence

In order to obtain a clean, well-ordered surface the sample was sputtered by Ne^+, $3\,\text{keV}$, and subsequently annealed to $750\,°\text{C}$ as described earlier. The arsenic was deposited by e-beam evaporation.

While investigating the system by HAS the adsorption of As (at constant flux) was monitored by recording the intensity of the specular (reflected) beam. Two representative deposition curves are shown in figure 6.1. The first one was recorded with the sample at room temperature. There is a sharp decrease in intensity once the shutter to the evaporator is opened. Beyond a certain coverage, the specular intensity decreases very slowly. If the sample is held at about $200\,°\text{C}$, a similar linear reduction in specular intensity is observed at the beginning, but the intensity increases again, revealing the formation of an ordered adsorbate structure. Further adsorption of As again leads to a decrease in intensity.

In both cases, the evolution of the specular intensity strongly differs from that observed for Sb and Bi on the same surface. The linear decrease indicates the formation of islands on the substrate [54]. At elevated temperature (figure 6.1 (b)) an ordered adsorbate structure is found when the specular intensity reaches its local maximum. At this coverage, electron diffraction and helium diffraction exhibit Bragg peaks which are located at the same bulk derived positions as the clean surface (see figure 6.2 (b)).

Since quasicrystalline adsorbate structures have been discussed in the previous chapter, the focus of the following part lies on the changes upon further heating. After annealing to about $550\,°\text{C}$, new diffraction spots appear as indicated by arrows in figure 6.2 (c) and by red circles
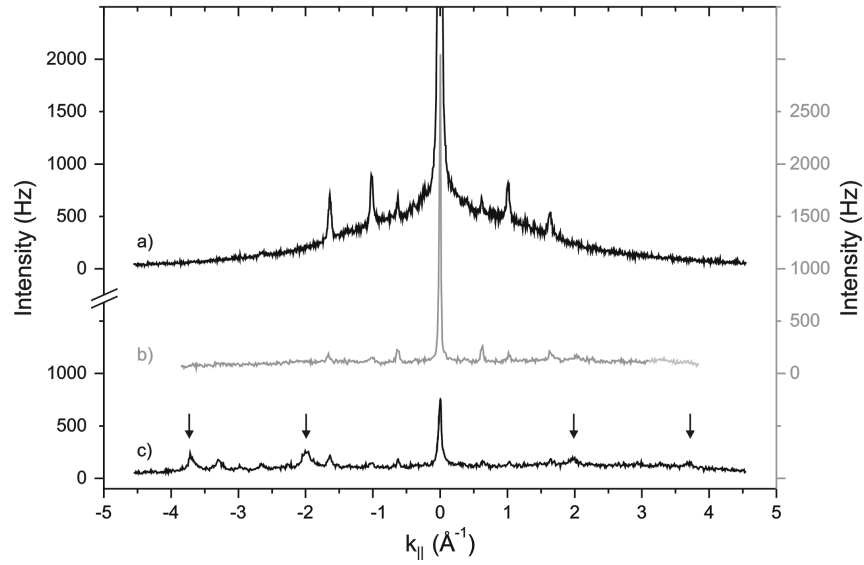
Figure 6.2: Helium diffraction spectra along the [10000]-direction of (a) the clean surface, (b) As deposited until the maximum in the adsorption curve of 6.1 (b), (c) preparation as in (b) and subsequent annealing to 550 °C.
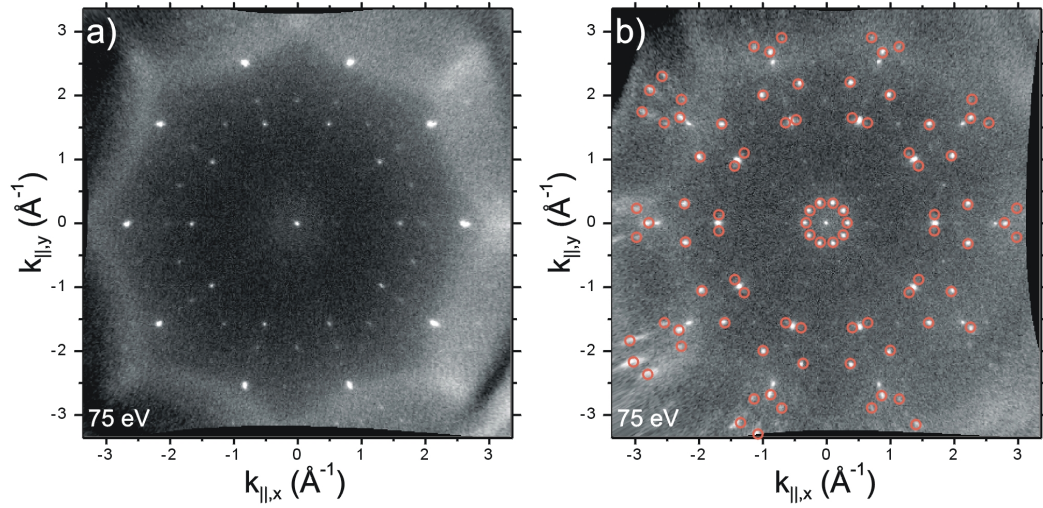

Figure 6.3: SPA-LEED pictures at 75 eV electron kinetic energy of (a) the clean tenfold d-Al-Ni-Co surface, (b) after As deposition and annealing. Peaks additionally observed to the Bragg points of the clean surface are marked by red circles. k_x and k_y are parallel to the quasicrystalline [10000]- and [001$\bar{1}$0]-direction, respectively. If not otherwise indicated, this will hold throughout this chapter.

in figure 6.3 (b). In contrast to the remaining Bragg peaks of the clean surface, these move with energy in the $\mathbf{k}_\parallel$-representation of the clean tenfold surface. This is a clear indication of the formation of facets as will be explained in the subsequent section. Annealing up to 750 °C does not remove this structure. Deposition of more As (which incidentally yields a further decrease of helium specular intensity in the adsorption curve) and subsequent annealing to 550 °C again produces the same structure. In order to obtain estimates about the As coverage and its stability at high temperatures, the experiments in the SPA-LEED chamber were complemented by X-ray photoelectron spectroscopy (XPS). The starting point of systematic studies was a sample with many monolayers of As deposited at 150 °C which did not show any LEED pattern. While annealing up to 500 °C does not change the As coverage, a decrease of the As peaks in the XPS spectra is observable at 550 °C. At the same time a LEED pattern with strong facet spots appears. The last few monolayers are stable up to a temperature of 750 °C. Even at this temperature the As does not desorb completely and the facet structure is still present.

Deposition of large amounts of As onto the surface at about 550 °C, on the other hand, yields XPS spectra where only Al and As are identified, indicating the formation of thick AlAs layers. Comparing with the HAS data, one can conclude that one monolayer of As forms a quasicrystalline film on d-Al-Ni-Co, which is stable up to 550 °C. It then transforms into a stable facet structure. The amount of As retained in the facet structure is limited if the growth is preformed by deposition at low temperature and subsequent annealing at 550 °C, while preparation at high temperature allows a thicker facet structure, which is stable up to 750 °C.

It will be shown in the following that the facets consist of the well-known III-V semiconductor AlAs. The elevated temperature of 550 °C is therefore not only necessary to desorb excessive amounts of As, but also to maintain a sufficient mobility of Al to segregate to the surface.

The quasicrystalline As layer was not investigated by SPA-LEED because the formation is only possible by deposition of the exact coverage, since desorption attempts to remove excessive As always result in the facet structure.

6.2   Facet Orientation

In order to resolve the As-induced surface structure, SPA-LEED patterns in an energy range from 33 eV to 300 eV were recorded with $\mathbf{k}_\parallel$ parallel to the Al-Ni-Co(00001) surface. The obtained diffraction patterns were rescaled on the basis of the remaining diffraction spots of the clean surface to compensate for non-ideal characteristics in the octupole deflection unit. While these few weak peaks are stationary in this representation, the majority of spots moves with energy.
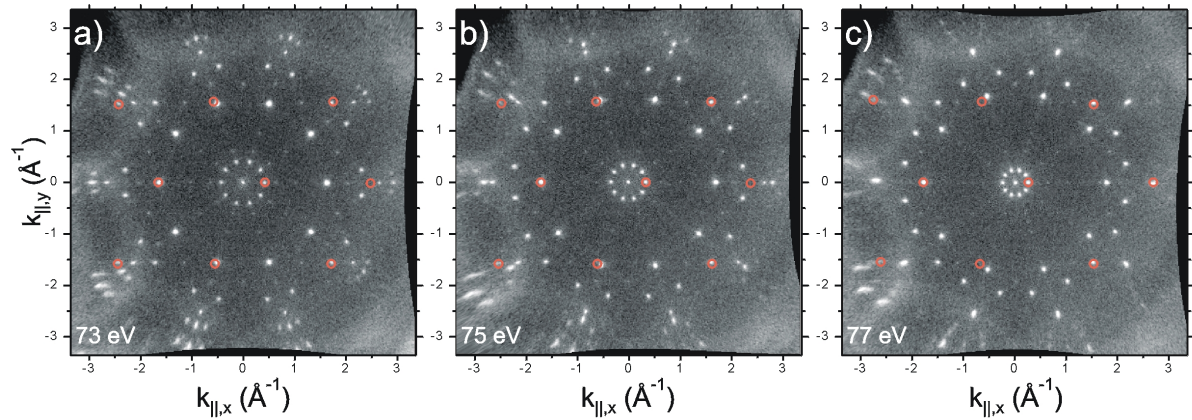
Figure 6.4: SPA-LEED patterns at (a) 73 eV, (b) 75 eV, and (c) 77 eV. Spots moving from right to left with increasing energy are marked by colored circles.
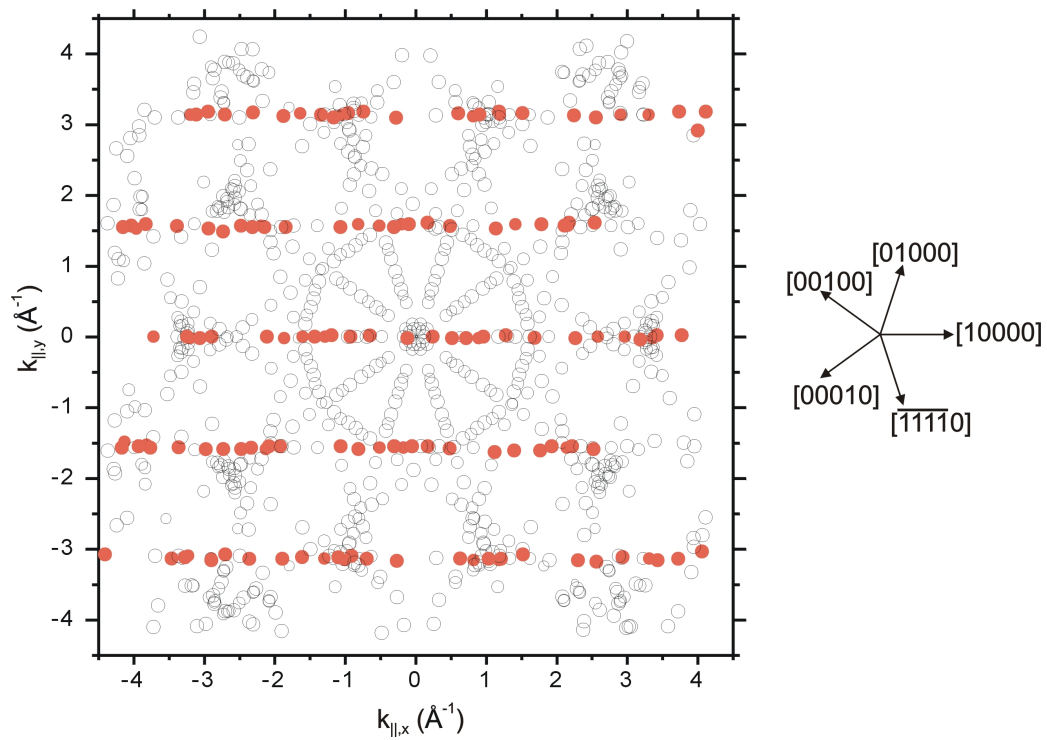

Figure 6.5: Schematic summary of the observed facet spots in the energy range from 100 - 200 eV in 10 eV steps. Bragg peaks belonging to one particular facet are marked by red circles. These move from right to left with increasing energy. The basis vectors of the d-Al-Ni-Co(00001) surface are given on the right hand side.

This means diffraction occurs from surfaces which are not parallel to the macroscopic surface. Consequently, their diffraction spots are located on facet rods which are inclined with respect to those of the clean surface. The direction of movement was followed by tracing the spot positions while changing the energy. For example, figure 6.4 shows three LEED patterns recorded at slightly different electron energy. One immediately recognizes the decreasing diameter of the inner ring of diffraction spots with increasing energy. An equivalent movement can be found for the other spots. One set of spots which shows equivalent behavior is indicated by red circles.

A summary of all observed facet reflections in the energy range from 100 - $200\,\text{eV}$ in $10\,\text{eV}$ steps is illustrated in figure 6.5. Diffraction spots of one particular facet are marked by red circles, while all others are black. With increasing energy the spots of the red set change their positions from right to left. Hence, facet spots moving along the [10000]-direction through $\mathbf{k}_\parallel$ and along parallel lines shifted by multiples of $(1.57 \pm 0.05)\text{Å}^{-1}$ are associated with the red set. An equivalent movement of facet spots with energy along the [01000]-,[00100]-,[00010]-, and [$\bar{1}\bar{1}\bar{1}\bar{1}0$]-direction is observed. Each of these directions has a mirror-symmetric counterpart moving along the same line in the opposite direction.

It is remarkable that the overall tenfold symmetry is preserved while the facets are obviously made up of a periodic structure. This only leaves the interpretation that the facets themselves are arranged in a tenfold symmetry. Contrary moving facet spots can be attributed to equivalent planes tilted in opposite direction. No stationary diffraction spots in addition to those of the clean surface can be found.

The angle of inclination of the facet planes can be obtained from a vertical cut in $\mathbf{k}$-space. For this, 2D diffraction patterns at various energies have been cut along the [10000]-direction. Taking into account the scattering geometry, gray-scale plots of these cuts yield the $\text{k}_\perp$ vs $\text{k}_\parallel$ plot depicted in figure 6.6. In this section of $\mathbf{k}$-space, there are three sets of parallel high intensity lines. One is visible for small $\text{k}_\perp$ values only. These lines are vertically running at $\text{k}_\parallel = \pm 1.65\,\text{Å}^{-1}$, and thus can be attributed to the clean tenfold surface. The other two sets of lines are tilted with respect to the former. Their angles of inclination can be measured directly from the plot. They are found to be $\pm (35.0 \pm 0.5)\,^\circ$. The facet rods within these sets are spaced periodically with a distance of $(1.80 \pm 0.10)\,\text{Å}^{-1}$.

While SPA-LEED provides the advantage of directly probing a two-dimensional section of the Ewald sphere, the disadvantage lies in a possible electrostatic distortion of the recorded patterns due to non-linearities in the deflection unit (which can be more or less corrected by calibrating the images using known diffraction patterns) and due to electric fields arising from differences in the work functions of the clean and the faceted surface region. Although these 'exterior' fields are assumed to be very small [112], a possible effect cannot be ruled out completely, such that a
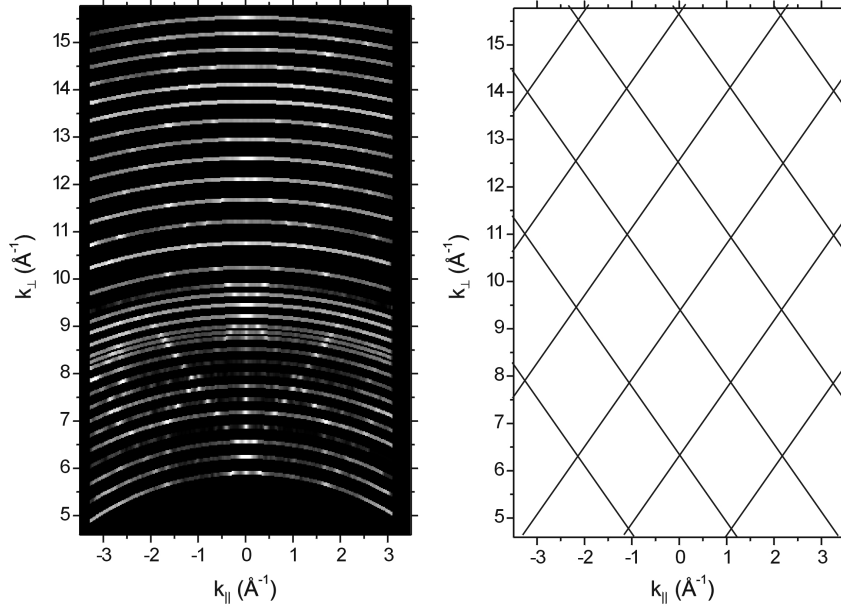
Figure 6.6: (a) Vertical cut of reciprocal space along the [10000]-direction after As deposition at 100 °C and annealing to 550 °C. (b) Schematic illustration of the facet rods observed in (a).

systematic error in the determination of the inclination angle might be present. By employing Helium atom scattering influences of electrostatic effects are avoided, but imaging of the entire Ewald sphere is not practicable. However, the angle of inclination of the facet planes can be determined by recording the elastic scattering at varying angle of incidence of the He atoms. Figure 6.7 shows helium diffraction spectra recorded along the [10000]-direction, i.e., along the inclination of the facets. Unfortunately, in part (a) of this figure the angle of incidence of the helium atoms was not chosen large enough to directly observe the reflected beam of the facet planes. The inclination angle therefore has to be determined by the first and second order diffraction spots. Starting with their Bragg conditions (recall that the sampled Ewald sphere possesses a radius of $\sqrt{2}k_i$)

$$b_1^* = \sqrt{2}k_i \sin(\alpha_1 - \alpha_0) \tag{6.1}$$

$$2b_1^* = \sqrt{2}k_i \sin(\alpha_2 - \alpha_0) \tag{6.2}$$

for the first and second order diffraction spot, respectively, one finds

$$\alpha_0 = \arctan\left(\frac{2\sin\alpha_1 - \sin\alpha_2}{2\cos\alpha_1 - \cos\alpha_2}\right) \tag{6.3}$$

where α_0, α_1 and α_2 denote the angle between the macroscopic specular and the zeroth, first and second order diffraction peak of the facet, respectively, and k_i is the absolute value of incident
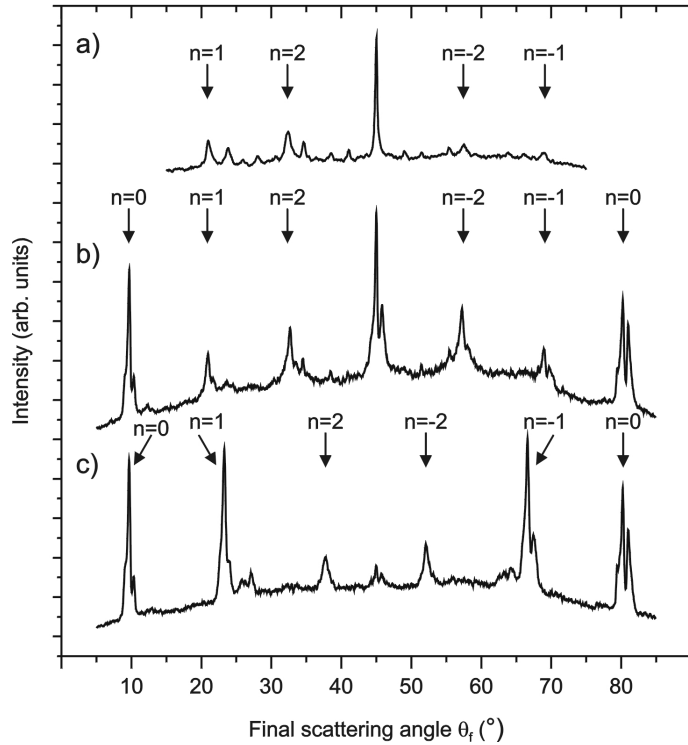
Figure 6.7: Helium diffraction spectra as a function of $\Theta_f = 90° - \Theta_i$ of the faceted d-Al-Ni-Co surface along the [10000]-direction of (a) a mono-grain sample at 21.6 meV beam energy, (b) a sample with multiple grains at 21.6 meV beam energy, (c) the same sample as in (b) at 15 meV beam energy. The facet spots are indicated by arrows and labeled by their respective order n.

wave vector. α_0 is the inclination angle of the facet rods. Analysis of several spectra at various energies yields a mean value of $\bar{\alpha} = (34.95 \pm 0.10)°$ and $\bar{b}_1^* = (1.76 \pm 0.01)\text{Å}^{-1}$.

However, one source of a systematic experimental error needs to be considered: In case of a uniform sample, a change of impact location of the He beam on the surface can occur unnoticed. This could result if the center of rotation of the sample does not lie in the surface plane where the beam hits the sample. Such a misalignment implies that the total scattering angle is not exactly $90°$ anymore and any measured angles are in error. The aperture in front of the detector limits the detected range to $0.25°$. Assuming that the alignment is only as good as this detector range leads to a larger error in inclination angle than derived above. Hence, $\bar{\alpha} = (34.95 \pm 0.35)°$.

In an effort to correct the displaced rotation of the sample, a sample with many quasicrystalline grains slightly tilted with respect to each other was investigated. Two spectra of such a sample at different energy are shown in figure 6.7(b) and (c). Each diffraction peak is split into two separate peaks and a shoulder on the left of this doublet. Comparison of the shape of all

twinned peaks allows to align the sample in a way that the displacement of the impact of the He beam from the rotation point of the sample is minimized and angles can be determined more accurately. In the present case, the described shape indicates that two rather large grains and several small grains contribute to the diffraction. The size of the large grains can be estimated by the size of the He beam on the sample, to be about $2\,\mathrm{mm}$. (The aperture in front of the nozzle was chosen to have a diameter of $0.6\,\mathrm{mm}$, such that the beam on the sample is $5.13\,\mathrm{mm}$ in diameter under an incident angle of $45°$). Observing a variation of the intensity ratios of these two peaks, implies a small change in beam position on the sample. If this is assumed to be less than $2\,\mathrm{mm}$, then the projected movement ($2\sin(80°)$) is of the same order and the error in angle amounts to $0.14°$. Since in this case the reflected beam from the facets was directly observed as the sample was rotated to smaller and larger angles of He incidence, the inclination angle of the facets can be determined directly. From a set of spectra at different energies the obtained value is $\bar{\alpha} = (35.27 \pm 0.14)°$ with a higher accuracy than derived from the SPA-LEED data. The reason for this detailed discussion is that this high accuracy of the inclination angle will be substantial for the determination of the atomic structure at the interface. The corresponding basis vector along the facet gradient yields $\bar{b_1}^* = (1.77 \pm 0.02)\text{Å}^{-1}$.

6.3 Atomic Structure

It has been shown in the previous section that all facet spots can be associated with ten different planes, each of which is inclined along a main symmetry line of the tenfold d-Al-Ni-Co surface by an angle of $\alpha = (35.27 \pm 0.14)°$. Moreover, it had been realized that the facets are built up of a periodic structure with basis vector b_1^* along the facet inclination ($b_1^* = (1.77 \pm 0.02)\text{Å}^{-1}$) and the perpendicular projection $b_{2,\mathrm{proj}}^* = (1.57 \pm 0.05)\text{Å}^{-1}$. From the large size of these basis vectors a rather simple structure with only a few atoms per unit cell can already be inferred.

In order to determine the structure in more detail, the distribution of facet spots of one particular facet plane, representative of all ten, was analyzed. The symmetry resembles a distorted hexagonal lattice as can be seen in figure 6.8, here for the plane inclined by $\alpha = (35.27 \pm 0.14)°$ with respect to the surface normal. Considering that the observed spots are the projection of the facet rods cutting the Ewald sphere, all distances between neighboring spots become smaller when cutting the sphere at large slope, and larger when cutting at negative slope, as illustrated in figure 6.9(b). Therefore, a hexagonal lattice is distorted in this representation of the SPA-LEED patterns.

Since As crystallizes in a rhombohedral structure with lattice parameter $a = 4.13\,\text{Å}$, and $\alpha = 54.17°$ [112], this bulk model does not match the observed structure. Moreover, the vapor
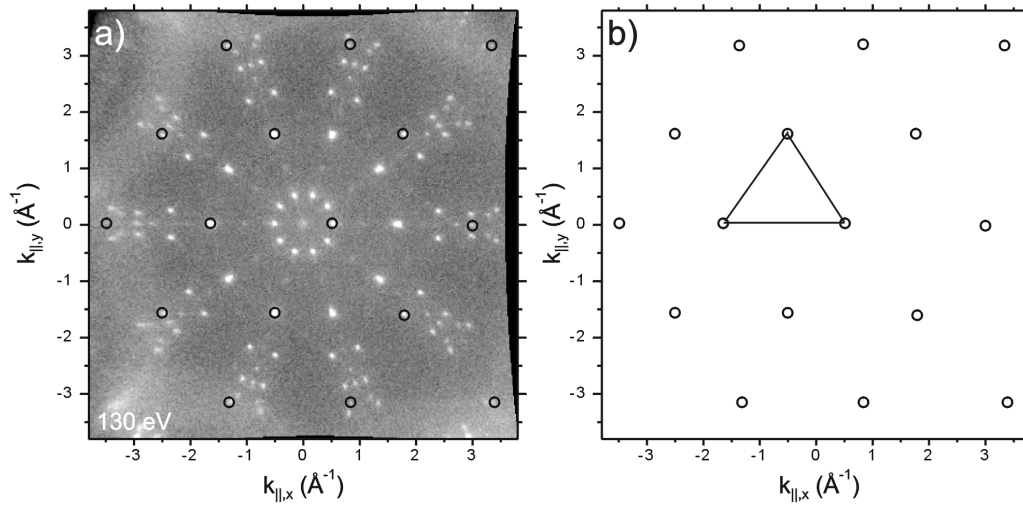
Figure 6.8: (a) SPA-LEED pattern of the As faceted d-Al-Ni-Co surface at 130 eV. Facet spots of one particular plane are encircled. (b) Marked facet spots from (a).
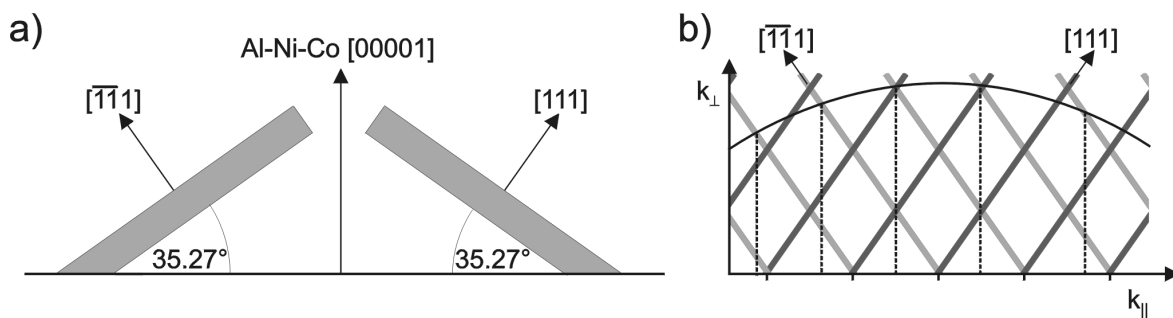

Figure 6.9: (a) Schematic cross section of the facet orientation. (b) Corresponding lattice rods in reciprocal space. The sector of the circle represents the sampled Ewald sphere, the dashed lines the projection of the cut of the dark grey facet rods with the sphere.
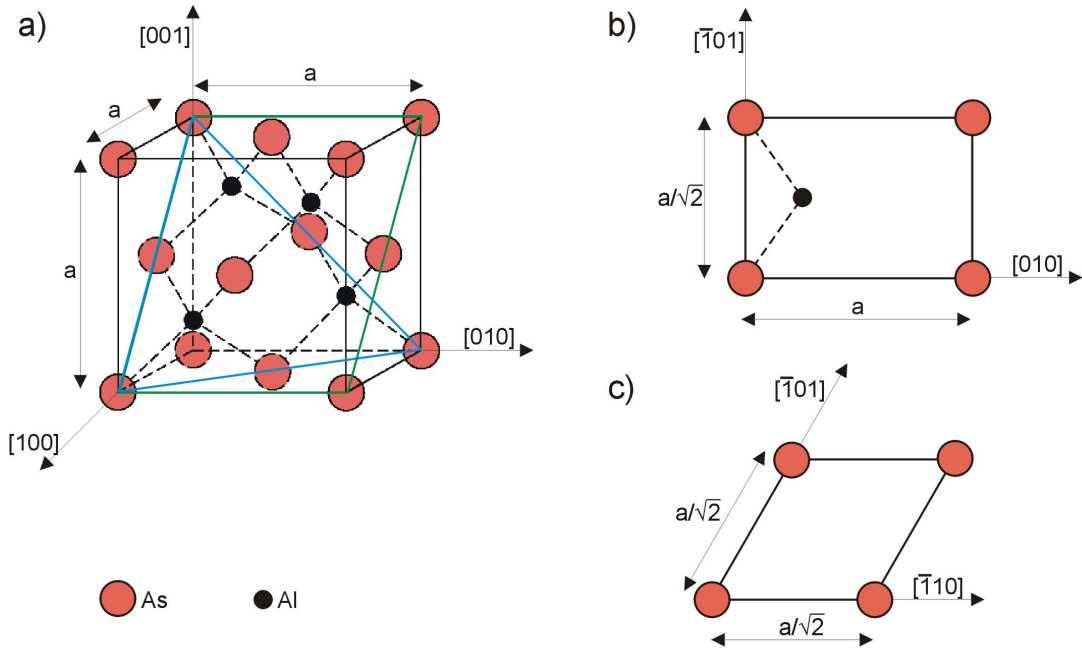
Figure 6.10: (a) Sphere model of the zinc-blende unit cell. The lattice consists of two interpenetrating face-centered cubic lattices displaced by one quarter of the diagonal length. Each sublattice is occupied by one atomic species, here Al and As. The (101) and (111) face are framed by green and blue lines, respectively. (b) Model of the (101) surface unit cell. (c) Model of the (111) surface unit cell.

pressure of As is 1330 mbar at 630 °C [124] which is much too high to allow for a stable phase in UHV up to 750 °C. In any case, also the XPS analysis had already indicated the formation of an AlAs alloy.

AlAs exhibits a zinc-blende crystal structure, with a lattice parameter of a = 5.62 Å [112]. The zinc-blende structure can be regarded as two interpenetrating fcc lattices displaced by a quarter of the volume diagonal. The atomic structure of the bulk unit cell as well as (101)- and (111)-unit cells are shown in figure 6.10(a-c), respectively. The hexagonal (111)-lattice thus possesses the reciprocal lattice vectors $\frac{1}{2}a^*_{(\bar{1}10)} = \frac{1}{2}a^*_{(\bar{1}01)} = 1.83 \text{Å}^{-1}$, and consequently $\frac{1}{2}a^*_{(\bar{1}01),proj} = \frac{1}{2}a^*_{(\bar{1}01)}\cos(30°) = 1.58\text{Å}^{-1}$. Hence, the bulk expected theoretical length of b^*_2 lies within the experimental error bar of $\frac{1}{2}a^*_{(\bar{1}01),proj}$, while the experimentally derived lattice vector $b^*_1 = (1.77 \pm 0.02)\text{Å}^{-1}$ is somewhat smaller than the bulk value of $\frac{1}{2}a^*_{(\bar{1}10)}$. In order to explain this deviation of the reciprocal lattice, which is related to a real space distortion, the interface between the periodic AlAs and the quasicrystalline substrate is analyzed in more detail in the following.

6.4   Interface Structure

The basic question is, whether the interface between a quasicrystalline and a periodic material can be long-range ordered and if so, how the stabilization is achieved. Interfaces between periodic crystals are well studied and characterized. Already in 1928 it had been observed that crystals grow with well defined orientational relationships with respect to each other, suggesting a matching of the atomic structure at the interface [125]. Macroscopic interfaces with aligned crystal orientations were henceforth named epitaxial. Over the years, the term epitaxy has been refined to describe atomic relations. Epitaxial growth is nowadays understood as a matching of lattice parameters between substrate and adsorbate [126]. In contrast to epitaxy stands the incommensurate growth, in which the ratio of lattice parameters of the substrate and adsorbate is irrational [124].

In general, stable interfaces between solids are expected if the total energy is minimized. In the case of incommensurate crystals, the interface energy is not changed upon displacing the lattices laterally with respect to each other. However, a shift of the adsorbate lattice on a commensurate substrate lattice yields a change in interface energy. The interface is stabilized in a local minimum of the interface energy.

In the simplest case, the minimum of the interface energy is expected if both lattices are in their equilibrium, i.e., bulk structure, and no interfacial bond-straining between the lattices occurs. Clearly, this can only be fulfilled if both solids are of the same lattice structure and parameter (e.g., in homoepitaxial systems), and the adsorbate can grow by maintaining the substrate structure as well as its own preferred bulk structure. However, also in systems with a misfit in lattice parameters, epitaxial growth can be achieved. If the lattice parameter mismatch with the substrate is less than about $9\,\%$, the film elastically strains at the interface to have the same interatomic distances as the substrate [126]. This growth mode is called pseudomorphic. In the case of a rough film, the strain can be reduced by a relaxation towards the bulk structure in higher layers. Otherwise, the arising elastic strain energy is lowered by the introduction of dislocations, which separate relaxed domains. In both described cases, the structures are commensurate and the diffraction patterns coincide. The same applies if the lattice parameters are multiples of each other.

An explanation of a stable structure at the periodic-to-quasiperiodic interface by these mechanisms is ad hoc not possible. Due to the lack of translational symmetry in quasicrystals the interface to the periodic AlAs cannot be described by a misfit in lattice parameters. The interface could at first sight be called incommensurate in the sense that the atom positions in the neighboring layers are not related by any well-defined distance to each other and none of the introduced effects can explain the structure. However, analysis of the diffraction patterns of the

respective interface layers points to a similar stabilization mechanism as will be shown.

6.4.1 A General Interface Model

In the case of commensurate adsorbate growth, the diffraction patterns of two periodic solids have a common lattice (plus possible superstructure spots). Thus, by inspection of the diffraction patterns, a straightforward judgment whether a stable long-range interface between the substrate and adsorbate can be formed is possible.

In contrast, quasicrystalline diffraction patterns consist of densely spaced Bragg points. In order to resolve the relation of arbitrary reciprocal lattices at the interface, a general approach from the interface energy leading to the reciprocal lattices of arbitrary structures is developed.

Let $\rho_1(r)$, $\rho_2(r)$ be the atomic densities of a substrate and adsorbate lattice, respectively. For simplicity, the potential $V_1(r)$ of the substrate is represented by a Gaussian function g at all atomic lattice sites, thus

$$V_1(r) = -(g * \rho_1)(r) . \tag{6.4}$$

The interface energy E can then be written as

$$E = \int \rho_2(r)V_1(r)dr \tag{6.5}$$

$$= \int \hat{\rho}_2(k_2) \exp(ik_2 r)\hat{V}_1(k_1) \exp(ik_1 r)dk_1 dk_2 dr \tag{6.6}$$

$$= -\int \hat{\rho}_2(k_2) \exp(ik_2 r)\hat{g}(k_1)\hat{\rho}_1(k_1) \exp(ik_1 r)dk_1 dk_2 dr \tag{6.7}$$

$$= -\int \hat{\rho}_1(k)\hat{\rho}_2(-k)\hat{g}(k)dk \tag{6.8}$$

where $\hat{V}(k)$, $\hat{\rho}_1(k)$, $\hat{\rho}_2(k)$, and $\hat{g}(k)$ are the corresponding Fourier transforms. The structure factors S are defined as the Fourier coefficients of the corresponding density distribution function. Thus, with the form factor f_n is set to unity,

$$E = -\int S_1(k)S_2(-k)\hat{g}(k)dk \tag{6.9}$$

with

$$S(k) = \sum_n \exp(ikr_n) . \tag{6.10}$$

However, the observable quantity is not the structure factor itself, but the intensity $I = S^*S$. Since $S(k)^* = S(-k)$ leads to $I(k) = I(-k)$ any asymmetry also for lattices of odd rotational symmetry is eliminated.

Hence, a criterion for a pronounced local minimum in the interface energy and therefore for epitaxy between arbitrary lattices is, that their diffraction patterns coincide in high intensity

Bragg points. Moreover, the Gaussian factor $\hat{g}$ in equation 6.8 weights Bragg points of small k-vectors more, which does not have any influence in periodic systems, but is of importance if at least one of the lattices is quasicrystalline.

6.4.2 One-Dimensional Example of Epitaxy between Periodic and Quasicrystalline Materials

In order to illustrate the above derived model in a one-dimensional case, the interface between a monoatomic periodic chain (with $f_n = 1$) and the common example for quasicrystallinity, the Fibonacci sequence, is presented in the following.

The structure factor of the periodic lattice yields

$$S_1(k) = \sum_n \delta(k - na^*) \tag{6.11}$$

with $a^* = \frac{2\pi}{a}$ the reciprocal lattice vector, while the structure factor of the Fibonacci sequence was derived in chapter 2 to be

$$S_2(k) = \sum_G \delta(k - G_\parallel) 2 \frac{\sin \frac{\Delta}{2} G_\perp}{G_\perp} \ . \tag{6.12}$$

Thus, the interface energy E of this system can then be written as

$$E \quad = \quad -\int \sum_n \delta(k - a^*n) S_2(-k) \hat{g}(k) dk \tag{6.13}$$

$$= \quad -\sum_n S_2(-a^*n) \hat{g}(a^*n) \ . \tag{6.14}$$

The minimization of the energy is thus achieved if a reciprocal vector of the Fibonacci sequence associated with a large structure factor coincides with a reciprocal vector of the periodic lattice.

Equation 2.17 and 2.18 yield the reciprocal basis vectors of the Fibonacci sequence. Their corresponding real space lengths are

$$a_{01} \quad = \quad \frac{2\pi}{G_{01}} = L(\tau + \frac{1}{\tau}) = \tau^2 \bar{a} \tag{6.15}$$

$$a_{10} \quad = \quad \frac{2\pi}{G_{10}} = L(1 + \frac{1}{\tau^2}) = \tau \bar{a} \tag{6.16}$$

$$a_{11} \quad = \quad \frac{2\pi}{G_{11}} = L(\frac{1}{\tau} + \frac{1}{\tau^2}) = \bar{a} \tag{6.17}$$

with

$$\bar{a} = \frac{mL + nS}{m + n} = \frac{\tau L + S}{\tau + 1} = \frac{(3 - \tau)}{\tau} L \tag{6.18}$$
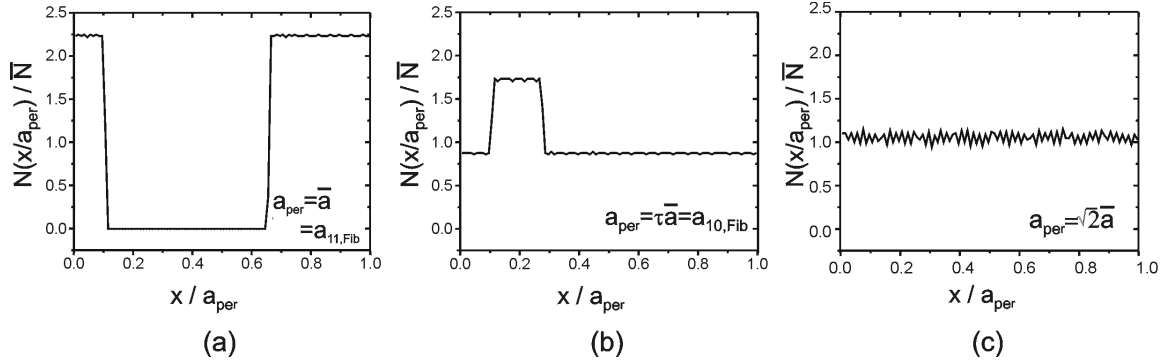
Figure 6.11: Periodic average structure of the Fibonacci sequence projected into (a) a unit cell with $a_{per} = \bar{a} = a_{11}$ corresponding to the strong Bragg peak G_{11}, (b) a unit cell with $a_{per} = \tau\bar{a} = a_{10}$ corresponding to the strong Bragg peak G_{10}, and (c) into a unit cell of parameter $a = \sqrt{2}\bar{a}$ not corresponding to any observable reciprocal lattice vector of the Fibonacci sequence. $N(x)$ is scaled by $\bar{N}$ which is the average number of nearest neighbors.

the average distance between the atoms. While a very low intensity is associated to G_{01}, already an intensity twice as large is related to G_{10} and again a more than doubled intensity corresponds to G_{11} [24]. In the following the real space structure of an interface between periodic lattices corresponding to the reciprocal vectors G_{10} and G_{11} and the Fibonacci sequence will be analyzed by calculating the nearest distance of the Fibonacci atoms from the atoms in the periodic chain.

For this, the Fibonacci sequence was generated by 18 inflations of the type $S \rightarrow L$ and $L \rightarrow LS$, resulting in 6765 atoms. The unit cell length of the periodic structure a_{per} was set to $a_{per} = \bar{a} = a_{11,Fib}$, $a_{per} = \tau\bar{a} = a_{10,Fib}$, and $a_{per} = \sqrt{2}\bar{a}$ which is not related to any observable reciprocal lattice vector of the Fibonacci sequence or its multiple. Then the distance of Fibonacci atoms to the nearest atom of the periodic chain is calculated. This corresponds to a projection of all Fibonacci atoms onto the periodic unit cell. Consequently, this distribution can be regarded as an average structure of a Fibonacci chain with respect to the periodic unit cell. Figure 6.11 shows these average distributions $N(x)$, henceforth referred to as the periodic average structure, i.e.,

$$N(x) = \frac{1}{N} \sum_{n-1}^{N} \rho_{Fib}(x - na_{per}) \ . \tag{6.19}$$

If a_{per} corresponds to a strong Bragg reflection, the periodic average structure is a distribution with a rectangular modulation containing a region with no atoms within the unit cell as illustrated in figure 6.11 (a). A periodicity related to a weak Bragg point leads to a weaker modulation of the Fibonacci atom distribution in the unit cell (figure 6.11 (b)), while a mismatch in reciprocal lattice vectors results in a distribution smeared out over the unit cell as in figure

6.11 (c).

Consequently, if the periodic lattice is chosen such that its Bragg reflections coincide with strong reflections of the Fibonacci sequence the corresponding average structure is localized in the unit cell of the periodic average structure. With the introduction of the periodic average structure the term epitaxy can be extended to a matching of the lattices or their periodic average lattices which are determined by strong Bragg reflections.

Steurer and Haibach have introduced the periodic average structure of quasicrystals in the higher dimensional concept [31]. An oblique projection of the atomic surfaces onto physical space yields regions occupied by atoms in the periodic average structure. Therefore, such a projection of the atomic surfaces yields the non-zero regions of figure 6.11 (a).

6.4.3   Periodic Average Structure of d-Al-Ni-Co

Having discussed a one-dimensional example of a periodic to quasicrystalline interface, these insights will now be applied to AlAs on Al-Ni-Co. For the moment, the surface of d-Al-Ni-Co is assumed to be flat. As the AlAs(111) facets are inclined by $(35.27 \pm 0.14)°$ with respect to the surface, the (101)-planes would in this case form the interface layer.

Figure 6.12 shows a calculated diffraction pattern of one plane of the tenfold surface of d-Al-Ni-Co superimposed on the diffraction pattern of the AlAs(101)-interface, which is aligned with its [010]-direction along the [10000]-direction of the substrate. The bulk expected rectangular lattice consists of the basis vectors with length $a^*_{(010)} = 1.12\,\text{Å}^{-1}$ along the [010]-direction and $a^*_{(\bar{1}01)} = 1.58\,\text{Å}^{-1}$ along the [$\bar{1}$01]-direction (marked by red circles in figure 6.12), while the experimental values yield a lattice with $b^*_{(011)} = \frac{b^*_1}{2\cos\alpha} = (1.08 \pm 0.02)\,\text{Å}^{-1}$ (with $b^*_1 = (1.77 \pm 0.02)\,\text{Å}^{-1}$ the reciprocal vector on the facet along its inclination and $\alpha = 35.27 \pm 0.14°$ the inclination angle) and $b^*_{(\bar{1}01)} = (1.57 \pm 0.05)\,\text{Å}^{-1}$ (marked by blue circles in figure 6.12).

The very intense substrate reflections $(110\bar{1}0)$, (01210), $(\bar{1}\bar{1}010)$, and $(0\bar{1}\bar{2}\bar{1}0)$ are matched exactly by the (22)-, $(\bar{2}2)$-, $(\bar{2}\bar{2})$-, and $(2\bar{2})$-facet spots, respectively, of the experimentally determined lattice, while the corresponding bulk derived spots deviate by 3.7%. The same holds for the comparison of the $(10\bar{2}\bar{2}0)$- and $(\bar{1}0220)$-points with the (40)- and $(\bar{4}0)$-diffraction peaks of the adsorbate. The (02)- and $(0\bar{2})$-spots in both cases fit very well with quasicrystal reflections $(011\bar{1}\bar{1})$ and $(0\bar{1}\bar{1}11)$.

The distortion of the bulk expected AlAs lattice towards the experimentally derived AlAs(101) plane, which matches the quasicrystalline Bragg points of high structure factor better, indicates an epitaxial growth mode as derived in sections 6.4.1 and 6.4.2. Similarly to the periodic average structure of the one-dimensional Fibonacci sequence discussed above, a periodic average structure of a two-dimensional quasicrystalline plane, such as the tenfold plane of d-Al-Ni-Co,
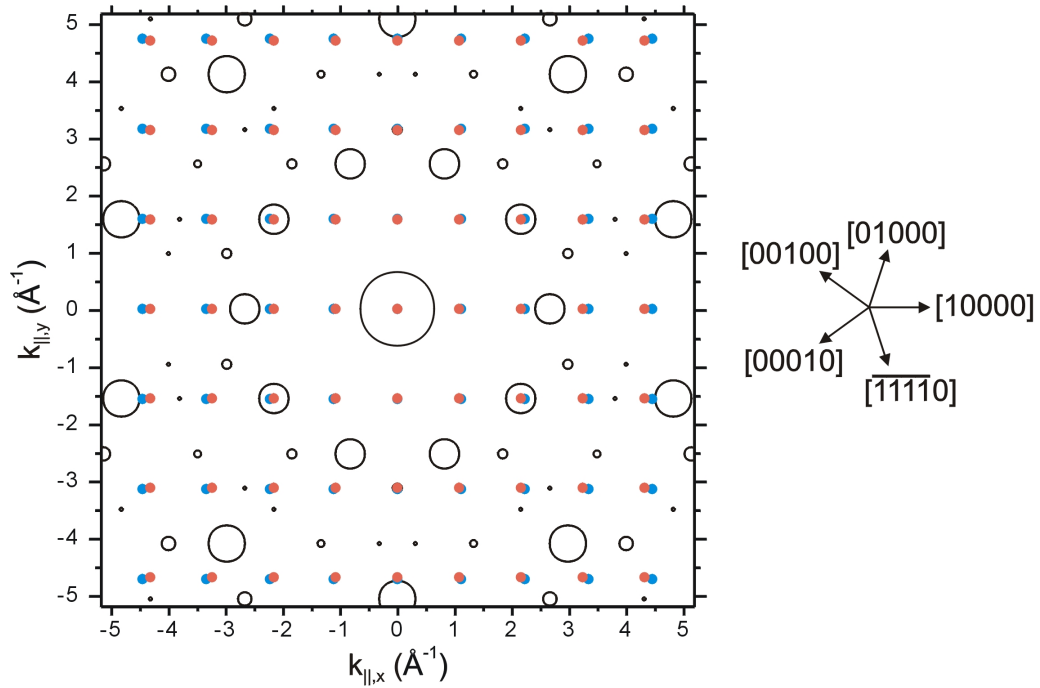
Figure 6.12: Calculated diffraction patterns of the quasicrystalline surface (black) [32, 57], the bulk expected AlAs (101)-interface (blue), and the experimentally derived (101)-AlAs interface (red). Basis vectors of the d-Al-Ni-Co surface are indicated on the right. The diameter of the circles in the quasicrystalline diffraction pattern scales with the intensity. For the periodic lattices only the positions, not the relative intensities of the Bragg peaks, are shown. They all have the same arbitrary diameter.

can be derived. Its periodic average structure can be obtained by a projection of the atomic distribution in the quasicrystalline plane onto a two-dimensional unit cell. In analogy to the one-dimensional case, unit cell dimensions corresponding to strong Bragg reflections lead to a strongly modulated distribution function while arbitrary lattice parameters not coinciding with Bragg points of the quasicrystal yield a homogeneous distribution of atoms in the unit cell. Hence, a periodic average structure related to strong Bragg reflections is again essential for epitaxial growth. Thus, the criterion for epitaxy is the matching of the adsorbate's reciprocal lattice with high intensity reflections of the quasicrystal as shown for the one-dimensional case in the previous section. Consequently, the AlAs adsorbate structure on d-Al-Ni-Co(00001) can already be termed epitaxial, and the real space implications are discussed in the following.

Steurer et al. have calculated the main periodic average structure of d-Al-Ni-Co [42]. It can

be regarded as a 5-lattice (i.e., the union of five sets of equivalent lattices rotated by $2\pi/5$ with respect to each other) of centered orthorhombic lattices with reciprocal lattice parameters

$$q^*_{(100)} \quad = \quad q^*\tau(\tau^2/2, 0, 0) \tag{6.20}$$

$$q^*_{(010)} \quad = \quad q^*\tau(0, \tau\sqrt{3-\tau}/2, 0, 0) \tag{6.21}$$

$$q^*_{(001)} \quad = \quad c^*(0, 0, 1) \tag{6.22}$$

with the basis vectors $q^* = 1.02\text{Å}^{-1}$ and $c^* = 1.54\text{Å}^{-1}$, $q^*_{100} = 2.16\text{Å}^{-1}$, $q^*_{010} = 1.57\text{Å}^{-1}$, and $q^*_{001} = 1.54\text{Å}^{-1}$. The corresponding real space unit cells, whose values are given in table 6.1, are superimposed on a section of the quasicrystalline plane in figure 6.13. In order to place the unit cells on a surface section of the quasicrystalline plane shown in figure 6.13, the projection of all lattice points onto the [001$\bar{1}$0]-direction (corresponding to the y-axis in the figure), and separately onto the [10000]-direction (x-axis) has been investigated. The projection onto the [001$\bar{1}$0]-direction yields broad distributions of lattice points separated by well-defined gaps. The projected lattice along the [10000]-direction is defined on narrower streaks, which are clearly separated from each other. Along this direction, the atomic positions are restricted to narrow areas. The periodic average structure can thus be identified, though a shift by half a lattice parameter along either direction yields an equivalent lattice as the lattice is base centered orthorhombic.

A comparison of the average periodic quasicrystalline structure with the AlAs(101) lattice cell then yields a perfect match of one adsorbate unit cell with two periodic average structure unit cells of the substrate, as illustrated in figure 6.14. However, also the measured lattice vector of AlAs perpendicular to the tenfold plane $b_{(101)} = 2b_{(010)}\tan\alpha = (4.10\pm0.06)$ Å matches the layer spacing of the substrate, i.e., $q_{(001)}$. Table 6.1 gives a compilation of the observed and theoretical lattice parameters. Therefore, the three-dimensional unit cell of the observed distorted AlAs facets is a multiple of the periodic average structure of the quasicrystal. Hence, any parallel alignment of the indicated lattice vectors would yield epitaxial growth.

In the following, it will be shown that he (10$\bar{2}\bar{2}$4)-plane and not the tenfold (00001)-plane of d-Al-Ni-Co that constitutes the interface to AlAs. Consider the lattice parameters in table 6.1: Clearly, the observed unit cell is distorted along x with a tensile strain of $(3\pm1)\%$. Assuming the matching with the periodic average structure of the substrate as derived above, the tensile strain amounts to 3.2 % and 0.8 % along x and y, respectively. Consequently, with the elastic response a reduced lattice constant along the z axis $b_{(101)}$ with respect to the bulk value $a_{(101)}$ is expected. However, this is not the case, indicating a different interface plane and therefore a faceting of the substrate.

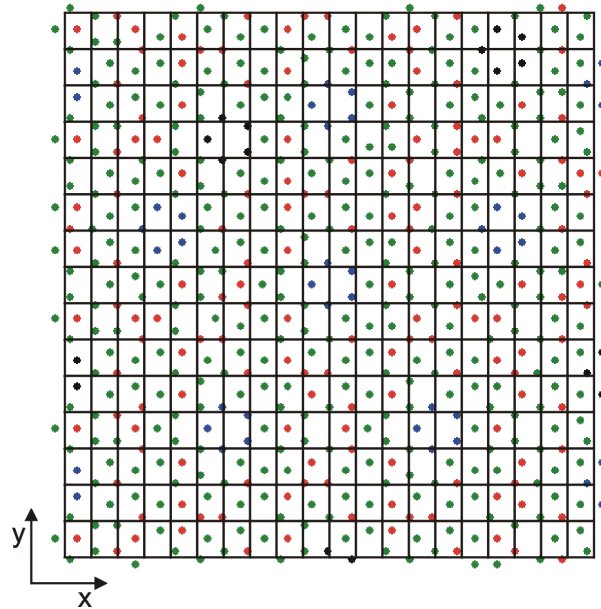Since no other facet spots aside from the ten sets associated with the AlAs($\bar{1}$11) facets are

Figure 6.13: Atomic distribution in a d-Al-Ni-Co plane. Al atoms are marked by green circles. Red, blue, and black circles represent transition metals. The grid indicates the unit cells $(4.00 \times 2.90)\text{Å}^2$ of the periodic average structure.
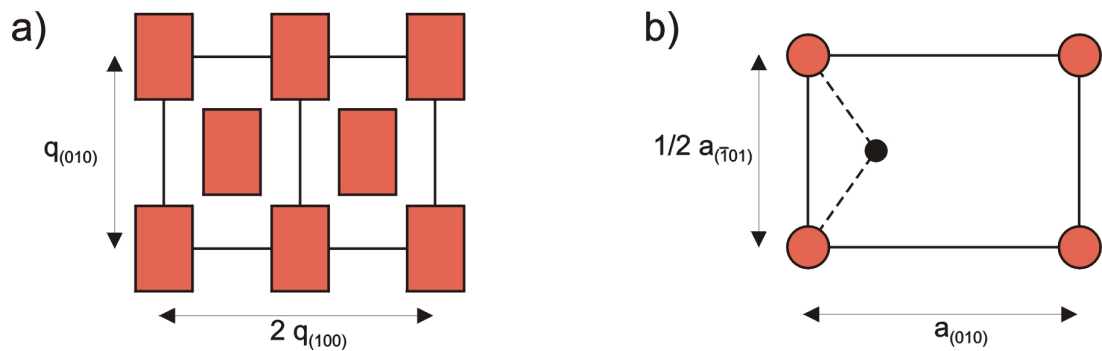

Figure 6.14: (a) Two unit cells of the periodic average structure. The rectangles indicate the elongated shape of the atomic distribution within the average unit cell. (b) Unit cell of the AlAs(101).

	Observed AlAs	Bulk expected AlAs	Periodic Average Structure of d-Al-Ni-Co
x	$b_{(010)} = 2 \times (2.90 \pm 0.04)\text{Å}$	$a_{(010)} = 2 \times 2.81\text{Å}$	$q_{(100)} = 2.90\text{Å}$
y	$b_{(\bar{1}01)} = 2 \times (4.00 \pm 0.15)\text{Å}$	$a_{(\bar{1}01)} = 2 \times 3.97\text{Å}$	$q_{(010)} = 4.00\text{Å}$
z	$b_{(101)} = 2 \times (4.10 \pm 0.06)\text{Å}$	$a_{(101)} = 2 \times 3.97\text{Å}$	$q_{(001)} = 4.08\text{Å}$

Table 6.1: Observed and theoretical real space lattice parameters of AlAs and the periodic average structure of d-Al-Ni-Co, x, y, z denote the coordinate axes: x is located within the tenfold plane and points along the inclination, y lies in the tenfold plane perpendicular to the inclination, and z is the surface normal.
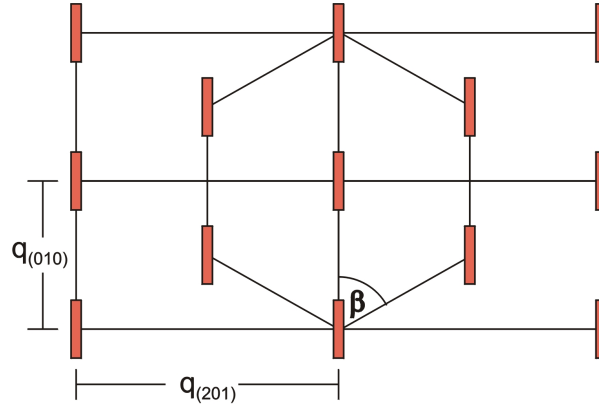

Figure 6.15: Unit cells in the (102)-plane of the periodic average structure of d-Al-Ni-Co. The rectangles illustrate the atomic distribution within the unit cells. The distorted hexagon with an angle $\beta = 60.57°$ corresponds to the distorted AlAs(111) unit cell.

observed, the only remaining possibility for the interface plane is an Al-Ni-Co facet parallel to the AlAs(111) surface. Any other inclination of the substrate would yield an additional set of facet spots. For example, if the AlAs(111) layer grows on a quasicrystalline facet of inclination angle γ the twofold symmetry of this plane would yield an additional facet with inclination angle $2\gamma - \alpha$. The absence of quasicrystalline facet spots on planes parallel to the AlAs(111) surface even at low coverage is readily explained: Their facet rods are parallel to those of AlAs(111) and therefore their strongest diffraction spots coincide with those of AlAs at all energies.

The $(10\bar{2}\bar{2}4)$-plane of Al-Ni-Co is inclined by $\alpha = \arctan \frac{2\tau q^*}{4c^*} = 35.14°$ (with $q^* = 1.0236\,\text{Å}^{-1}$ and $c^* = 1.5398\,\text{Å}^{-1}$ [120]) with respect to the (00001)-plane. The inclination direction is along [00001]. Hence, this plane is parallel to one set of the observed AlAs(111) facet planes. Moreover, it corresponds to the (102)-plane of the periodic average structure. Consequently, $b_{(11\bar{2})}$ is aligned

with $q_{(\bar{2}01)}$ of the periodic average structure at the interface. The same holds for $b_{(\bar{1}10)}$ and $q_{(010)}$. The structure of the (102)-plane of the periodic average structure is illustrated in figure 6.15. The atomic distribution within the unit cells resembles a hexagonal structure as indicated by the distorted hexagon in figure 6.15. The AlAs(111) unit cells are locked into registry with these lattice points of the periodic average structure. Therefore, a tensile strain of 3.2 % and 0.8 % along AlAs(11$\bar{2}$) and AlAs($\bar{1}$10), respectively, is accumulated, but the matching of the adsorbate lattice with the periodic average structure of the substrate stabilizes the long-range ordered interface. Due to the inplane tensile stress a small inward relaxation perpendicular to the facet's surface is expected. The SPA-LEED or HAS experiments, however, are not sensitive to detect such a perpendicular relaxation.

6.5   Facet Size

In the previous section a long-range order within the facets had already been inferred from the observation of diffraction. A more quantitative description of facet sizes can be gained by spot profile analysis of the diffraction peaks. The profile of the facet spots in the SPA-LEED images is elongated along the gradient of the facet planes as shown in figure 6.16(a) for a (20)-facet spot at $E = 65\,\mathrm{eV}$ and $k_\parallel = 1.35\,\text{Å}^{-1}$. A Gaussian profile was fitted along the elongation and perpendicular to it, yielding a clear difference in the full-width at half maximum of $w_\parallel = (0.0556 \pm 0.0005)\,\text{Å}^{-1}$ and $w_\perp = (0.0325 \pm 0.0005)\,\text{Å}^{-1}$. However, before drawing final conclusions on the facet dimensions, geometric effects need to be considered. A significant elongation might arise from the inclination of the facet rod, thus producing an elliptical cross section when cut by the Ewald sphere. The correction for this geometric effect can be obtained by

$$w_{\parallel,corr} = \frac{w\cos(\alpha \pm \beta)}{\cos\beta} \text{ with } \beta = \arcsin(\frac{k_\parallel[\text{Å}^{-1}]}{1.023 \cdot \sqrt{E[eV]}}) \tag{6.23}$$

where w is the measured width of the facet spot and α the inclination angle of the facet rods. Evaluation of the facet spots by this correction yields a slightly narrower facet rod width along the radial direction of $w_{\parallel,corr} = (0.0508 \pm 0.0005)\,\text{Å}^{-1}$. The minimum average facet size therefore amounts to 120 Å and 200 Å along and perpendicular to the inclination, respectively. It should be noted that the facet width is dependent on the preparation method and coverage. However, this example shows that a long-range ordered interface can be formed.
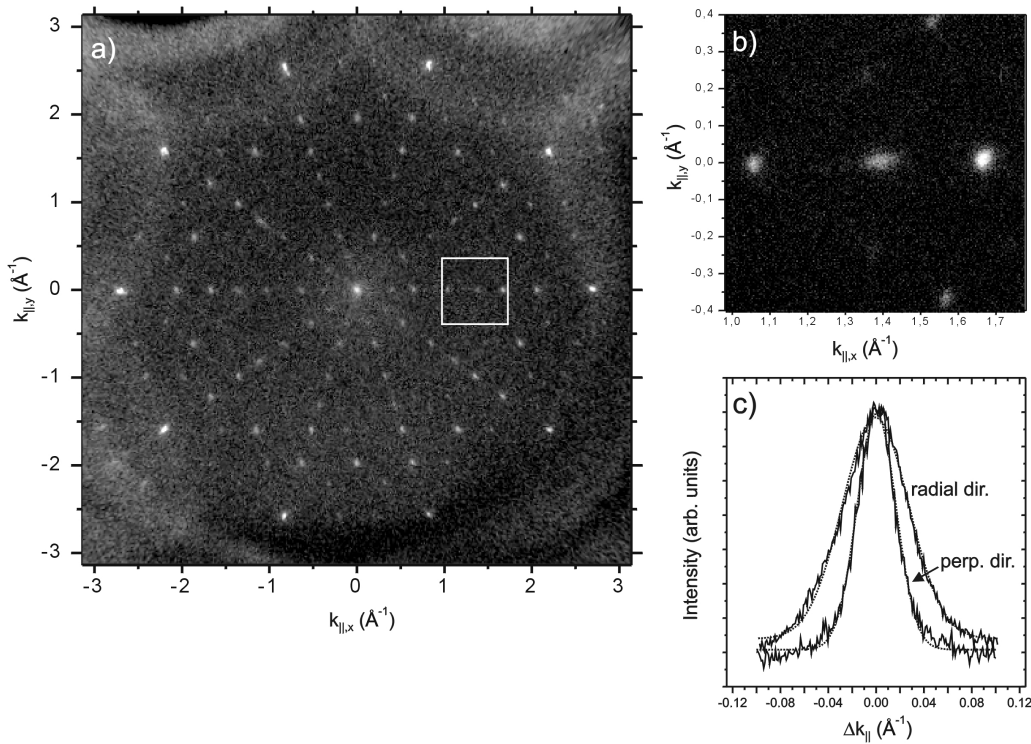
Figure 6.16: (a) SPA-LEED pattern at 65 eV. The white rectangle marks the section recorded with higher resolution in (b). (b) 2D spot profile of a 2nd order facet spot at 65eV. (c) Spot profile of (b) (solid line) fitted with a Gaussian profile (dashed line) along the radial and perpendicular direction.

6.6 Conclusions

In conclusion, As forms a quasicrystalline monolayer like Sb and Bi on the tenfold surface of d-Al-Ni-Co. In contrast to the observations for Sb and Bi, this film is only metastable and transforms into a facet structure upon annealing to temperatures higher than about $500\,°C$. The overall tenfold symmetry is conserved by tenfold symmetrically arranged facet planes of at least $200\,\text{Å} \times 120\,\text{Å}$ size. The facets are oriented perpendicular to $[10\bar{2}\bar{2}4]$-equivalent axes. They are covered by a film of the well-known III-V AlAs compound in its zinc-blende structure. The interface plane is parallel to the facet planes and the AlAs film grows in (111)-orientation. The film's unit cells are enlarged by $3.2\,\%$ along the $[01\bar{2}]$-direction as compared to the bulk lattice.

The tensile strain is necessary to achieve a matching of the AlAs lattice with the main periodic average structure of the substrate at the interface. With the introduction of the concept of the

periodic average structure and its identification by strong reflections in the diffraction pattern a generalization of epitaxial growth on substrates of aperiodic long-range order is obtained.

Finally, the question remains why As behaves differently from Bi and Sb. For Bi, the question is answered easily: Bi desorbs at about $450\,°\mathrm{C}$ which is too low to allow a sufficient mobility of Al to segregate to the surface. For Sb, on the other hand, it could be possible to obtain an AlSb alloy in a narrow temperature range. However, its lattice parameter of $6.14\,\mathring{\mathrm{A}}$ yields basis vectors $a^*_{(\bar{1}01)} = 1.02\,\mathring{\mathrm{A}}^{-1}$ and $2a^*_{(010)} = 1.45\,\mathring{\mathrm{A}}^{-1}$ in the quasicrystalline plane, which match well with the (10000) reflection, but deviate significantly from all other strong quasicrystalline lattice points. Thus, a distortion to compensate the differences would need to be too large to be energetically stable. Indeed, in search for such a structure no epitaxial periodic film has been found.